Astronomy & Astrophysics

Eruptions from coronal bright points: A spectroscopic view by IRIS of a mini-filament eruption, QSL reconnection, and reconnection-driven outflows[*]

Maria S. Madjarska[1][ORCID], Duncan H. Mackay[2][ORCID], Klaus Galsgaard[2][ORCID], Thomas Wiegelmann[1], and Haixia Xie[3]

[1] Max Planck Institute for Solar System Research, Justus-von-Liebig-Weg 3, 37077 Göttingen, Germany
e-mail: madjarska@mps.mpg.de
[2] School of Mathematics and Statistics, University of St Andrews, North Haugh, St Andrews KY16 9SS, Scotland, UK
[3] Fundamental Teaching Department, Shandong Jiaotong University, 264209 Weihai, Shangong, PR China

ABSTRACT

Context. Our study investigates a mini-filament eruption associated with cancelling magnetic fluxes. The eruption originates from a small-scale loop complex commonly known as a coronal bright point (CBP). The event is uniquely recorded in both the imaging and spectroscopic data taken with the Interface Region Imaging Spectrograph (IRIS).
Aims. The investigation aims to gain a better understanding of the physical processes driving these ubiquitous small-scale eruptions.
Methods. We analysed IRIS spectroscopic and slit-jaw imaging observations as well as images taken in the extreme-ultraviolet channels of the Atmospheric Imaging Assembly (AIA) and line-of-sight magnetic-field data from the Helioseismic Magnetic Imager (HMI) on board the Solar Dynamics Observatory. As the observations can only indicate the possible physical processes at play, we also employed a non-linear force-free field (NLFFF) relaxation approach based on the HMI magnetogram time series. This allowed us to further investigate the evolution of the magnetic-field structures involved in the eruption process.
Results. We identified a strong small-scale brightening as a micro-flare in a CBP, recorded in emission from chromospheric to flaring plasmas. The mini-eruption is manifested via the ejection of hot (CBP loops) and cool (mini-filament) plasma recorded in both the imaging and spectroscopic data. The micro-flare is preceded by the appearance of an elongated bright feature in the IRIS slit-jaw 1400 Å images, located above the polarity inversion line. The micro-flare starts with an IRIS pixel size brightening and propagates bi-directionally along the elongated feature. We detected, in both the spectral and imaging IRIS data and AIA data, strong flows along and at the edges of the elongated feature; we believe that these represent reconnection outflows. Both edges of the elongated feature that wrap around the edges of the erupting MF evolve into a J-type shape, creating a sigmoid appearance. A quasi-separatrix layer (QSL) is identified in the vicinity of the polarity inversion line by computing the squashing factor, Q, in different horizontal planes of the NLFFF model.
Conclusions. This CBP spectro-imaging study provides further evidence that CBPs represent downscaled active regions and, as such, they may make a significant contribution to the mass and energy balance of the solar atmosphere. They are the sources of all range of typical active-region features, including magnetic reconnection along QSLs, (mini-)filament eruptions, (micro-)flaring, reconnection outflows, etc. The QSL reconnection site has the same spectral appearance as the so-called explosive events identified by strong blue- and red-shifted emission, thus providing an answer to an outstanding question regarding the true nature of this spectral phenomenon.

Key words. Sun: filaments, prominences – Sun: activity – Sun: chromosphere – Sun: corona – methods: data analysis – methods: numerical

1. Introduction

Over the past few years, we reported three studies on eruptions from small-scale loop systems known as coronal bright points (CBPs) by Mou et al. (2018, hereafter Paper I), Galsgaard et al. (2018, hereafter Paper II), and Madjarska et al. (2018, hereafter Paper III). These eruptions have been labelled as jets in extreme-ultraviolet (EUV) and X-ray data (e.g. Madjarska et al. 2020, and references therein) when detected in coronal holes and mini coronal mass ejections (mini-CMEs, Innes et al. 2009; Mou et al. 2018) observed in the quiet Sun. The term mini-CME is used to describe the observation of small-scale eruptions that do not evolve as collimated flows, namely, as jets that are typically ejected from CBPs in coronal holes. Rather, these events

develop as expanding bubbles due to the closed magnetic-field structure of the quiet Sun. Whether these eruptions are fully confined or some of the ejected material reaches the interplanetary space remains an open question. We refer hereafter to this phenomenon simply as 'mini-eruptions'. The CBPs are composed of a set of small-scale coronal loops seen with enhanced emission in EUV and X-rays linking photospheric magnetic-flux concentrations of opposite polarity (for review see Madjarska 2019).

Here, we briefly review the main results on the eruptions from Papers I, II, and III. Firstly, Paper I shows that 76% of the analysed CBPs (31 out of 42) were the source region of one or more eruptions. The eruptions generally occurred during the late stage in the life of the CBPs, which is when magnetic-flux convergence and cancellation are typically occurring. The CBP eruptions commonly evolve with the ejection of cool and hot plasma. The cool plasma appears in absorption in the coronal
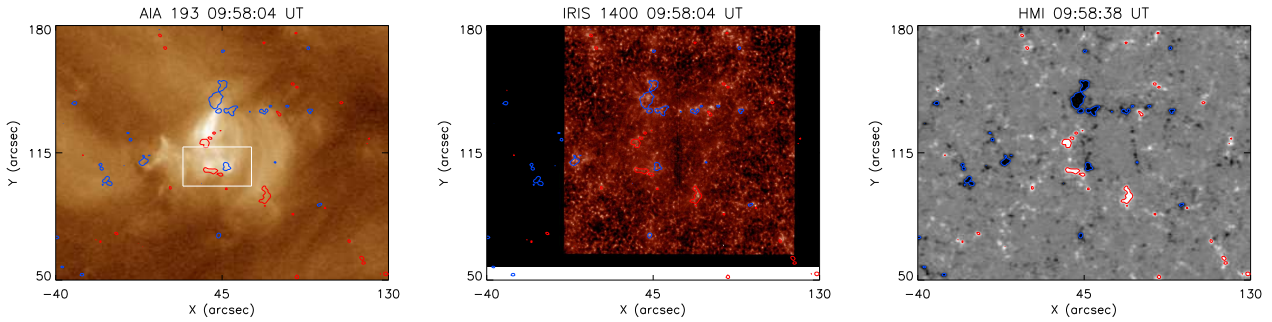

Fig. 1. Small-scale loop system known as a coronal bright point. *Left to right*: AIA 193 Å, IRIS SJI 1400, and HMI magnetogram images with the CBP in the centre of the field of view (FOV). The red and blue contours trace magnetic fluxes at ±50 G. The HMI magnetograms are saturated at ±50 G. The white-line square in the first panel outlines the FOV shown in Fig. 2.

imager channels and is related to mini-filaments (MFs), while the hot plasma represents the expelled CBP loops and the overlying corona. Micro-flares always appear at the CBP polarity inversion line (PIL) during CBP eruptions. We identified dimmings caused by MF's 'dark' appearance and reduced emission due to density depletion. In Paper II, we proceeded with the non-potential time-dependent modelling of the CBP magnetic field. A non-linear force-free field (NLFFF) relaxation approach using a time series of Helioseismic and Magnetic Imager (HMI) line-of-sight magnetograms was employed. Details on the methodology can be found in Sect. 4 of Paper II and Appendix A of Paper III. The results reveal that most of the CBP eruptions in Paper II are related to the formation of twisted magnetic flux, namely, flux ropes that form at the location of the eruptions. The nature of the micro-flares have remained unclear and it was investigated in Paper III, where a large CBP located in an equatorial coronal hole was studied. In this study, it was found that the formation and destabilisation of mini-filaments cause the occurrence of a EUV/X-ray jet. The mini-filament formed along the polarity inversion line of the CBP 3−4 h before its eruption seen in GONG (Global Oscillation Network Group) Hα images. In this case, the bipolar magnetic flux was not seen to converge or cancel during the time leading to the MF destabilisation and eruption. Most importantly, the eruption-associated micro-flare was identified with three flare kernels seen in the Hα images appearing shortly after the MF lift-off. The derived magnetic NLFFF model reproduced features explaining various observational characteristics related to the evolution of the CBP and the eruption of the MF.

In the present paper, we investigate a mini-filament eruption from a CBP associated with a micro-flare and cancelling magnetic fluxes. The Interface Region Imaging Spectrograph (IRIS) spectral and imaging observations capture the energy release site associated with the mini-eruption, revealing crucial information on how the magnetic reconnection and associated phenomena evolve in the course of the cancellation of bipolar features detected in magnetic-field observations. To shed more light on the configuration and evolution of the coronal magnetic field associated with the observed complex phenomenon and the physical processes that are taking place, we also employ a NLFFF relaxation modelling, followed by a squashing-factor computation. Section 2 reports on the observations from IRIS, Atmospheric Imaging Assembly (AIA), and HMI. The modelling methodology is given in full detail in Papers II and III. The observational and modelling results are presented in Sect. 3 and the discussion is given in Sect. 4. The summary and conclusions are presented in Sect. 5.

2. Observational data

On 5 April 2017, during a dedicated observing campaign of CBPs, IRIS (De Pontieu et al. 2014) took observations of a CBP located not far from the disc centre (see Fig. 1, first panel). The observations include slit-jaw images (SJIs) taken in the 1400 Å (hereafter SJI 1400) with a field-of-view (FOV) of $119'' \times 119''$ and 17 s cadence and a pixel size of $0.17'' \times 0.17''$. The IRIS spectral data were taken in a rastering mode with a 17 s cadence, and a 15 s exposure time. The width of the IRIS slit is $0.35''$ while the pixel size in solar Y is $0.17''$. Seven spectral windows were transferred to the ground. In this study, we analyse the Si IV 1393.75 Å line that has a maximum formation temperature of log $T(K) = 4.9$ as well as the optically thick C II 1334.53 Å and Mg II k 2796.35 Å lines that have more complex formation. In general, the Mg II[1] lines sample the mid-chromosphere (for details see Leenaarts et al. 2013), while C II the upper chromosphere and low solar transition region (Rathore et al. 2015). The C II[2] lines typically form above the Mg II lines.

We also analysed imaging data from AIA (Lemen et al. 2012) on board the Solar Dynamics Observatory (SDO) (Pesnell et al. 2012) taken in the EUV 94 Å (hereafter AIA 94), 193 Å (hereafter AIA 193), 171 Å (hereafter AIA 171), and 304 Å (hereafter AIA 304) channels. A description of the response of the EUV channels is given in Paper I and III, as well as in Madjarska et al. (2021). The AIA EUV data have a 12 s cadence and $0.6'' \times 0.6''$ pixel size. We used HMI line-of-sight magnetograms (Scherrer et al. 2012) that have both a 45 s and a 720 s cadence. The HMI data have a $0.5'' \times 0.5''$ pixel size but were rescaled to the AIA pixel size of $0.6'' \times 0.6''$ using the hmi_prep.pro procedure. The AIA 1600 Å images were used to align the HMI data with those from the EUV channels and IRIS with a precision of the alignment at ∼1''. All images were de-rotated to 10:00 UT on 5 April.

3. Results

The IRIS spectroscopic and imaging observations were taken in the far-ultraviolet (FUV) and near-ultraviolet (NUV) wavelength ranges, providing information about the physical properties and dynamics of the chromospheric and transition-region plasmas in the quiet Sun of the solar atmosphere. Combined with AIA transition-region and coronal imaging observations, these data give a complete overview of the emission from plasmas with a wide range of temperatures. Such an assembly of data can

---

[1] https://iris.lmsal.com/itn39/Mg_diagnostics.html
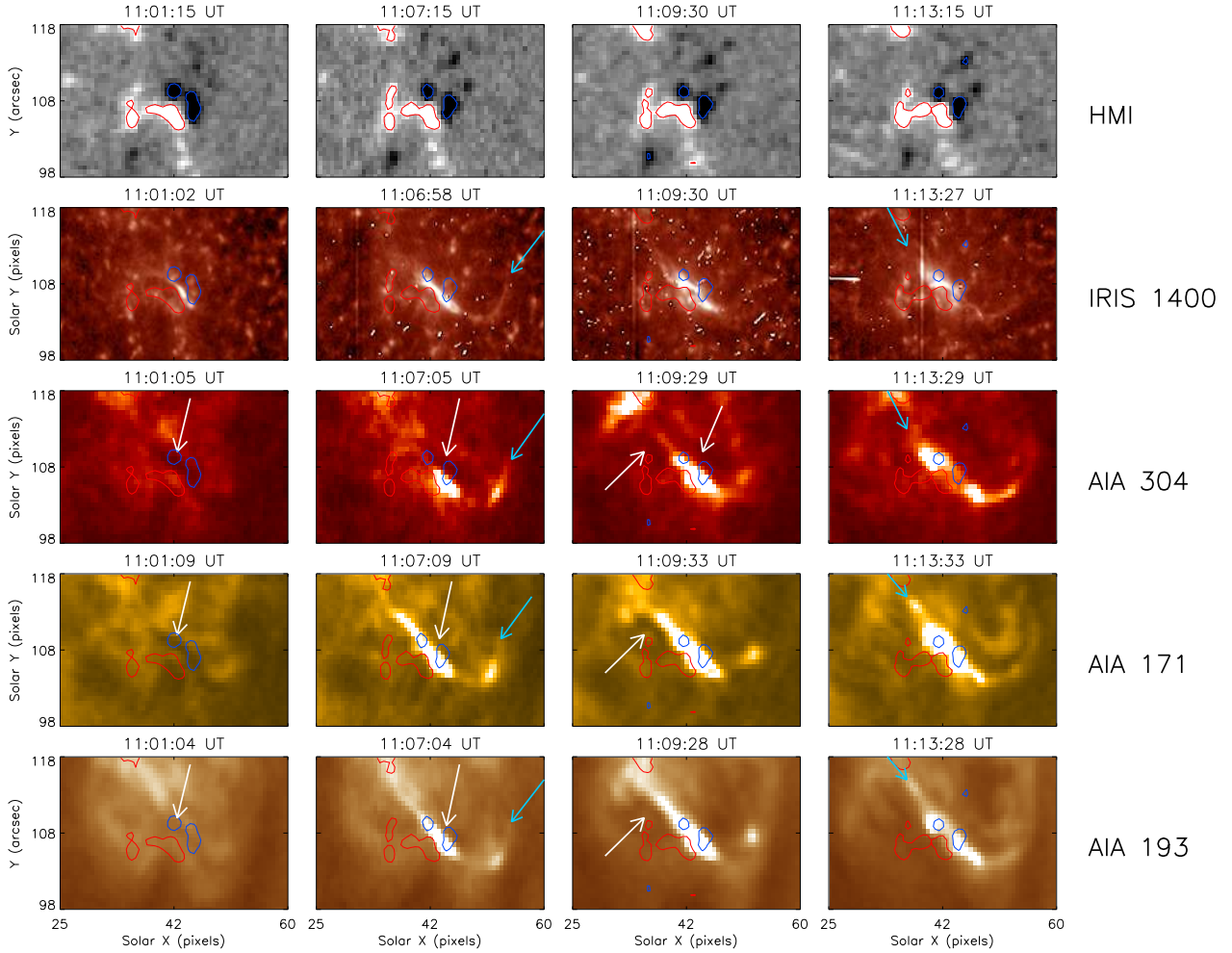[2] https://iris.lmsal.com/itn39/CII_diagnostics.html

Fig. 2. HMI magnetograms, IRIS SJI 1400, AIA 304, AIA 171, and AIA 193 images showing the evolution of the eruption (in order *from top to bottom*). The white arrows point at the mini-filament seen in absorption, i.e. the 'dark feature'. The red and blue contours trace magnetic fluxes at ±50 G. The cyan arrows indicate the hot plasma up-flows seen as bright extensions from the reconnection site.

sample emission from the upper photosphere in the AIA 1600 channel (together with some transition region emission from C IV lines), the mid and upper chromosphere (in e.g. Mg II and C II), up to emission from a flaring corona in the AIA 94 Å channel with a response of up to 7 MK (Fe XVIII, for details, see O'Dwyer et al. 2010; Del Zanna 2013).

As we mention in Sect. 2, the observations analysed here were taken during a dedicated CBP observing campaign when CBPs close to the disc centre were targeted. As the IRIS planning process requires a target selection a day in advance, it means that the observed CBPs would often be in the late stage of their lifetime given the fact that the CBP average lifetime is 24 h (see Sect. 3.2 in Madjarska 2019).

The first quick look at the AIA and IRIS data taken on 5 April 2017 indicated that during the second of the two IRIS rasters, both hot and cool plasma ejections occurred. The small-scale plasma ejection of cool plasma is associated with a mini-filament, while the hot plasma is linked to the bright point coronal loops and micro-flare heated plasmas taking place at the lower (southern) part of the targeted CBP. The source region of the eruption is shown in Fig. 1 in the centre of the area outlined with a white square. The evolution of the phenomenon can be followed in the animation provided in Figs. 2 and A.1, where near co-temporal multi-instrument images are shown. To the best of our knowledge, this is the first report of a mini-eruption from

a small-scale loop system (a CBP) in the quiet Sun involving a mini-filament that has been detected in the IRIS imaging (slit-jaw) and also in the spectral data; namely, the spectrometer slit is scanning the site while the eruption is ongoing.

At first glance, the evolution of the eruption in the high-resolution SJI 1400 appears very intriguing as certain details are revealed which have never been detected before in AIA images due to resolution limitations. The spectral observations revealed even more exciting features, as stronger blue- and weaker red-shifted emission were on display in all spectral lines while the slit was crossing the eruption site. This type of spectral appearance has typically been attributed to the so-called 'explosive events' (EEs) (e.g. Brueckner & Bartoe 1983; Dere et al. 1984) that are interpreted as the observational signature of bi-directional flows resulting from magnetic reconnection (e.g. Dere et al. 1991). We come back on this in Sect. 4. The co-temporal imaging information suggested a highly dynamically evolving eruptive phenomenon associated with a mini-filament eruption and a micro-flare (Innes et al. 2009). To inspect this we then analysed all available data including magnetic and intensity imaging (Sect. 3.1) and spectral (Sect. 3.2) observations. As observations can only provide an inkling of the possible physical processes in play, we also performed data-driven simulations (see Sect. 3.3) to obtain a deeper and more accurate insight into the physical processes involved in the observed phenomenon.

Table 1. Timeline of the eruption.

Time (UT)	Event
04:00	The bipole forms
05:30	Interconnecting loops seen in AIA 304
06:00	Cancellation starts
09:45	The magnetic flux of the bipole starts to decrease
11:00	Bright elongated feature along the PIL in SJI 1400
11:00	MF starts to appear in the AIA EUV channels
11:00:45	First brightening appears in SJI 1400
11:02:41	First brightening appears in AIA 304
~11:03	First brightening appears in AIA 193 and AIA 171
~11:04	First brightening appears in AIA 94
~11:06	Quick coronal intensity depletion
~11:06	MF lifts-off
~11:06	Outflows appear

3.1. Eruption in the imaging data

The source region of the eruption is a bipole. Its location is shown in the centre of the top row of the images in Fig. 2. The bipole opposite polarity fluxes arise from the convergence of the negative flux of a newly emerging bipole with a pre-existing positive flux concentration. The negative flux increases in strength while approaching the positive flux which remains relatively stationary. The region forms as a discernible bipole around 04:00 UT on 5 April. Interconnecting loops become distinguishable in the AIA 304 channel almost an hour and a half later, at ~05:30 UT. A few minutes later, interconnecting loops also appear in the high-temperature AIA 171 and 193 channels. The cancellation between the two opposite polarities starts at ~06:00 UT. Overall, CBPs are known to be formed by loops at different temperatures, where hotter larger loops are reported to overlie cooler lower ones (Madjarska 2019). The bipole total magnetic flux starts to decrease around 09:45 UT and falls sharply until at least 11:28 UT with a total absolute flux decrease of about 24%; thus, the measurable cancellation has started earlier than the eruption analysed here. The magnetic flux decrease is about 13% between the detectable beginning 10:59 UT and the end of the eruption at 11:28 UT. The timeline of the events can be followed in Table 1.

The transition-region and coronal activity above the bipole location begin around 09:30 UT with two mini-eruptions very similar to the one investigated in detail here. They are, however, weaker, especially in the AIA imaging data. The first eruptive event occurred during the time period between 09:40 UT and 09:55 UT (scanned by the IRIS slit) and the second between 10:15 UT and 10:25 UT (not scanned by the IRIS slit). Repetitive eruptions (homologous) from the same cancelling bipole are a very common feature and have been shown and discussed in detail in Mou et al. (2018) and Galsgaard et al. (2019).

The third in the series of eruptions is studied here in full detail. It begins with the appearance of a bright elongated feature (the same is seen during the first eruption) that can only be seen in the IRIS SJIs starting at 11:00 UT (see the animation in Fig. A.1). The feature extends above the polarity inversion line separating the two opposite polarities. It has a cross-section of approximately two IRIS pixels or 0.34″ (<250 km) which is one of the possible explanations for why this feature is only distinguishable in the IRIS data and not in the AIA data that have a pixel size of 0.6″ × 0.6″.

The dynamic event starts with a pixel size brightening at the elongated feature seen in the SJI 1400 at 11:00:45 UT that expands bi-directionally along the elongated feature. This type of brightening is considered to be the observational signature of a micro-flare. It first appears in AIA 304 at 11:02:41 UT. In the coronal channels AIA 193 and AIA 171 it is seen at 11:03:16 UT and 11:03:09 UT, respectively, which can be considered co-temporal given the fact that the two channels do not operate simultaneously. To determine with more certainty that the observed brightening is related to impulsive heating at a few million degrees (flare-type), we investigated the emission in the AIA 94 channel. This channel contains the Fe XVIII 93.932 Å line (maximum formation temperature of 7.08 MK) but also emission from spectral lines with lower formation temperatures like Fe X, XII, etc. Detailed information and analysis on this can be found in Del Zanna (2013). To remove the 'contamination' by the cooler emission we used the emission from the event in the AIA 211 and 171 channels. We subtracted this 'cooler emission' by applying the expression given by Del Zanna (2013). The resulting response in the AIA 94 can be followed in Fig. A.1 in the channel named AIA Fe XVIII. The plasma at the initial micro-flare location first reached very high temperatures at 11:04 UT. The micro-flare signature appears below the rising mini-filament as has been observed in our earlier cases of mini-eruptions (for more details and additional examples see Mou et al. 2018). Because of the obscuration caused by the rising MF (for more details see Mou et al. 2018; Madjarska et al. 2020), a light curve (not shown here) clearly demonstrates the presence of hot plasma only between ~11:06 UT and ~11:10 UT.

An inspection of the general evolution of the CBP (see the first panel of Fig. 1) indicates that the CBP as seen in AIA 193 on 5 April is part of a larger loop system with a configuration and evolution that appear intricate due to a complex distribution of magnetic flux at a photospheric level. In other words, the loops forming the CBP are not rooted in a simple bipolar region. This type of CBP has been described in our previous studies (see e.g. Mou et al. 2018), thus, we do not go into further details here.

A mini-filament starts to appear in the AIA EUV images around 11:00 UT (see the animation in Fig. A.1) and it becomes visible as an elongated absorption (dark) feature shortly before its eruption. The white arrows in the second and third columns in Fig. 2 point at the MF. An enlarged view is also given in the first panel of Fig. 3, left panel. The MF lies along the polarity inversion line (PIL) separating the bipole mentioned above. The appearance of the MF is not exactly between the two polarities, which can be explained by the asymmetry of the magnetic configuration (for more details, see Sect. 3.3). The MF has an apparent minimum length of 8.7 Mm, which is below the average size of mini-filaments at 11 Mm (15″) (Hermans & Martin 1986). As the filament length is determined in the coronal imaging data and not in the chromospheric line (e.g. Hα, see discussion on the visibility in Madjarska et al. 2020), the true length could be greater than the estimated one. After a slow rise between roughly 11:01 UT and 11:06 UT, the MF lifts off which can be followed in the time-slice images in Figs. 3 and A.1. The AIA 304 gives the best view of the MF eruption. Innes et al. (2010) using data from the twin EUVI (Extreme Ultraviolet Imager) of the SECCHI (Sun Earth Connection Coronal and Heliospheric Investigation) telescopes on the STEREO spacecrafts, namely, a combination of on-disk and off-limb data, have found that the removal of the overlying corona, seen as coronal emission depletion, occurs earlier than the rise of the MF. The dimming region is caused by reduced coronal density and the presence of the erupting mini-filament seen in absorption.
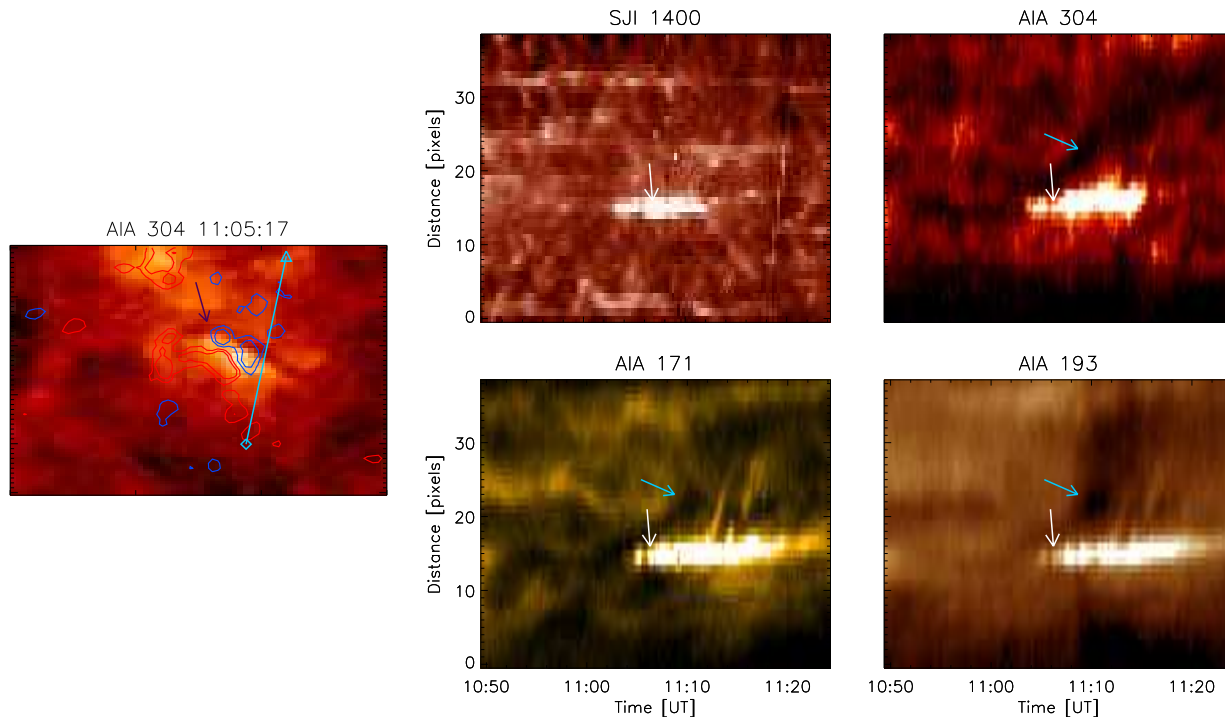
Fig. 3. Temporal evolution of the mini-filament eruption and micro-flare in time slice images. *From left to right*: AIA 304 image during the mini-filament appearance as a dark elongated feature. A cyan line marks the slice from which the time-slice images in the second and third columns are produced. The square indicates the bottom and the triangle, the top of the slice images. The black arrow points at the mini-filament. The red and blue contours trace magnetic fluxes at ±25 G and ±50 G. *Top middle*: IRIS SJI 1400 time slice image. The white arrow points at the micro-flare (the same for the AIA images). *Bottom middle*: AIA 171 time-slice image. *Top right*: AIA 304 time-slice image, and *bottom right*: AIA 193 time-slice image. The cyan arrows point at the dimming region. The IRIS pixels are rescaled to the AIA pixel size.

For the case of the eruption studied here, AIA 193 shows better the dimming region than AIA 171. The dimming is least visible in AIA 304 apart from the footpoint of the erupting mini-filament. The AIA 171 and especially the AIA 193 channel show a more extended dimming region earlier than the mini-filament eruption, which could be due to the removal of the overlying corona, as mentioned above. However, we cannot be certain of this assumption because of the strong background emission. It should be noted that a brighter feature runs across the dimming region that is best seen in AIA 171. It is possibly related to some of the CBPs expanding loops, as seen in many similar cases by Mou et al. (2018).

The most probable explanation for the different appearance of the dimming region in the different AIA EUV channels is related to the intensity of registered background emission and its temperature, and the level of coronal depletion at a given temperature during the eruption. The AIA 304 channel is dominated by transition-region emission. The AIA 171 channel also contains strong background emission at low temperatures (for details on the response of the AIA EUV channels, see Sect. 3 in Paper I). Thus, the dimming will generally have a different appearance in different EUV channels. Examples of various appearances of dimming regions can be seen in Mou et al. (2018) and Madjarska et al. (2020). The MF is not visible in the SJI 1400, only the micro-flare. Generally, filaments (prominences) emit at transition-region temperatures, which come from the so-called prominence-corona transition region (e.g. Cirigliano et al. 2004; Madjarska et al. 1999) that separates the cool plasma of the filament core from the hot corona and can be distinguished only when observed above the limb. On disc, when seen as filaments, the emission is far too weak in comparison to the background chromospheric and transition-region emission of the quiet Sun. That is why the erupting filament cannot be distinguished in the IRIS SJ 1400 channel.

As seen in SJI 1400, a brightening associated with a micro-flare, as mentioned above, spreads bi-directionally along the elongated feature until ~11:03 UT when both its edges rapidly (in 17 s) expand in length forming J-shaped edges (for details see the animation in Fig. A.1). The J-shaped edges give the whole feature the appearance of a sigmoid. The link between filament eruptions and CMEs in active regions and sigmoids' appearance in EUV and X-rays, has long been established (e.g. Rust & Kumar 1996; Green et al. 2011; Joshi et al. 2017; Gibb et al. 2014). The sigmoid-like feature coincides with the rise of the MF with the J-shaped edges wrapping around the two legs of the rising MF. This is a strong indication for the presence of a quasi-separatrix layer (QSL, Démoulin et al. 1996; Titov 2007). The spreading of the bright emission seen in all EUV channels has already been observed in larger CBP eruptions by Madjarska et al. (2020). It has been associated with the micro-flare ribbons that are seen here as one single feature (due to the event's small size and limited resolution) rather than two bright lanes as typically observed in large solar flares (Fletcher et al. 2011; Janvier et al. 2014; Benz 2017). The micro-flare ribbons are the actual footprints of a current layer that has formed along the QSL, extending from coronal to photospheric heights. Figure 7 in Janvier et al. (2014) nicely illustrates this.

Plasma outflows are observed at two edges of the elongated feature best seen in the IRIS SJ images (for details, see the animation in Fig. A.1). The physical nature of these outflows is discussed in Sect. 4. At 11:06 UT the west edge curves upwards (i.e. J-shaped), which coincides with the lift-off of the filament
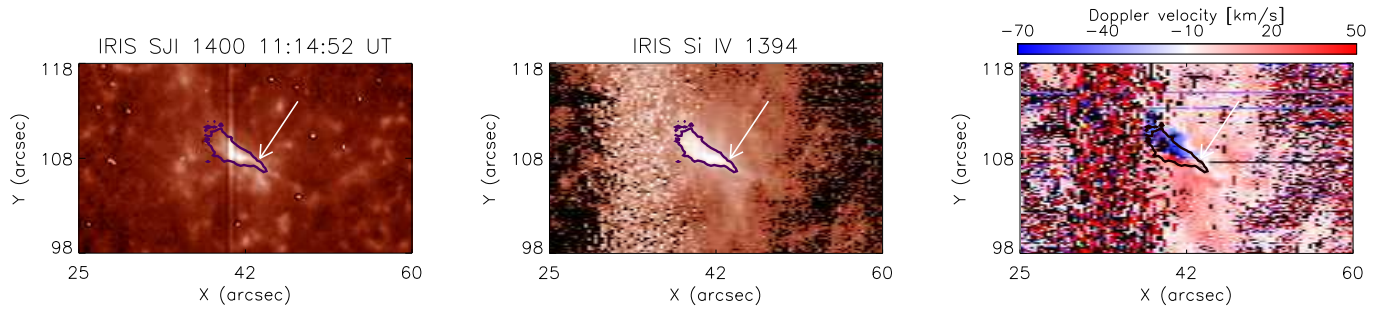
Fig. 4. IRIS SJI 1400 image, Si IV 1394 raster intensity, and Doppler velocity images (shown *left to right*). The contour outlines the micro-flare region in the Si IV 1394 raster image that is also overplotted on the SJI 1400 and Doppler-velocity images. The white arrow points at the reconnection site.

as mentioned above (following the animation in the AIA 304 and the SJ 1400 images). At 11:15 UT this extension and associated outflows are no longer visible in SJI 1400 but they remain present in the AIA 304 and coronal channels. The brightening along the whole structure starts to decrease after 11:10 UT initially from the west edge, close to where the initial brightening occurred while the eastern part continues being active. The elongated brightening event lasts at transition region temperatures until 11:31 UT (SJI 1400), while at the coronal one (AIA 171 and 193), it can be seen for at least another 10 min.

3.2. Eruption in spectroscopic data

The IRIS data provide a unique opportunity to investigate, for the first time, an erupting MF and associated phenomena in simultaneous imaging and spectroscopic observations. We analysed three of the recorded spectral lines, the chromospheric optically thick Mg II k 2796.35 Å (hereafter Mg II k 2796), and C II 1334.53 Å (hereafter, C II 1335) lines, and the transition region optically thin Si IV 1393.75 Å (hereafter, Si IV 1394) line. The Mg II k 2796 and C II 1335 have a complex formation and in the present event, the emission seen along the slit is even more intricate given the fact that it comes from plasmas that constitute an erupting filament, a reconnection site, and micro-flare ribbons (Madjarska et al. 2020). The central depression in the Mg II line is referred to as k_3, while the two peaks on of both sides are known as k_{2v} and k_{2r}. For simplicity, we refer to these peaks as blue and red wings.

Figure 4, right panel, displays the Doppler velocity image in the Si IV 1394 line obtained from a single Gaussian fit. It demonstrates a very clear image of a bi-directional flow that is centred above the polarity inversion line of the cancelling bipole. We obtained the reference wavelength from a line profile averaged over the entire data set that includes two raster scans. It should be noted that after the slit crosses the region indicated with the white arrow the dynamic event was already reaching its final moments. This is why the blue- and red-shifted emission are no longer detectable.

The IRIS slit first enters the eruption site seen as a bright elongated feature in the IRIS images after 11:12 UT (shown in the animation in Fig. A.2), while scanning the region from east to west. We can notice that the slit passes over the east J-edge of the elongated bright feature in the AIA 304 and 171 images (also AIA 193 in the animation in Fig. A.1), as early as 11:08 UT. Two minutes later this edge is obscured by the erupting mini-filament in the coronal EUV images. In the spectral data starting at 11:09:30 UT (shown in the animation in Fig. A.2), the mini-filament shows red-shifted emission first (around Solar Y 111″)

at just a few km s^{-1} in the Si IV 1394 and C II 1335 lines. Emission decreases in the red wing of Mg II k 2796 which probably indicates the expanding MF rather than falling down cool MF material. Unfortunately, the spatial resolution does not permit us to determine this with more certainty.

In Fig. 5, we display the emission in the three spectral lines at two times during the eruption, at 11:13 UT and 11:16 UT. During the 11:13 UT exposure, the slit crosses the east edge of the eruption and displays very complex emission and absorption line-shift patterns in the Mg II k 2796 line. We should note here that, generally, the filament cores have very low temperatures and thus their plasma is partially ionised. Together with their high density, this makes them optically thick to certain wavelengths, including Mg II k 2796 and C II 1335. The C II 1335 and the Si IV 1394 emission comes from the filament (prominence)-corona transition region (PCTR) (for details on the PCTR, see Parenti 2014). The MF is seen in absorption in the Mg II k 2796 line as its cool material absorbs the incident radiation which also happens in the C II 1335 line. At 11:13 UT in the Mg II k 2796 one can distinguish a decrease of the emission (an absorption feature) in the blue wing of the Mg II k 2796 line along the spectrometer slit (see the two black horizontal lines that mark the location along the slit where the filament is recorded) which indicates that cool material is lifting up (Doppler shifts of up to approximately 50 km s^{-1}). The same line shifts are also recorded in the C II 1335 and Si IV 1394 lines. Erupting large filaments have rarely been recorded in spectral data, but on these occasions, they were displayed with very large Doppler velocities of up to 300 km s^{-1} (e.g. Madjarska et al. 2015; Gömöry et al. 2016). Such an event was simultaneously registered in unique spectral SUMER (Solar Ultraviolet Measurements of Emitted Radiation on board the Solar Dynamics Observatory, SoHO) and CDS (Coronal Diagnostic Spectrometer/SoHO), and TRACE (Transition Region and Coronal Explorer) imaging observations. For details see Figs. 4–7 in Madjarska et al. (2015). A similar filament eruption was recorded in data from EIS (Extreme-ultraviolet imaging spectrometer) on board Hinode (see Fig. 5 in Gömöry et al. 2016).

During the 11:16 UT exposure, the blue-shifted emission associated with the filament is still present in the wing of the Mg II k 2796 data (intensity decrease in the wing, marked with the upper horizontal black lines in Fig. 5). We can also see a very strong blue-shifted wing in the Si IV 1394 line of more than 100 km s^{-1} and weaker in the C II 1335 line. We ought to be cautious, however, since at this slit position, the emission in the spectral data (especially in the transition region lines) is possibly composed of emission coming along the line of sight from both the mini-filament and the bright elongated feature. Red-shifted
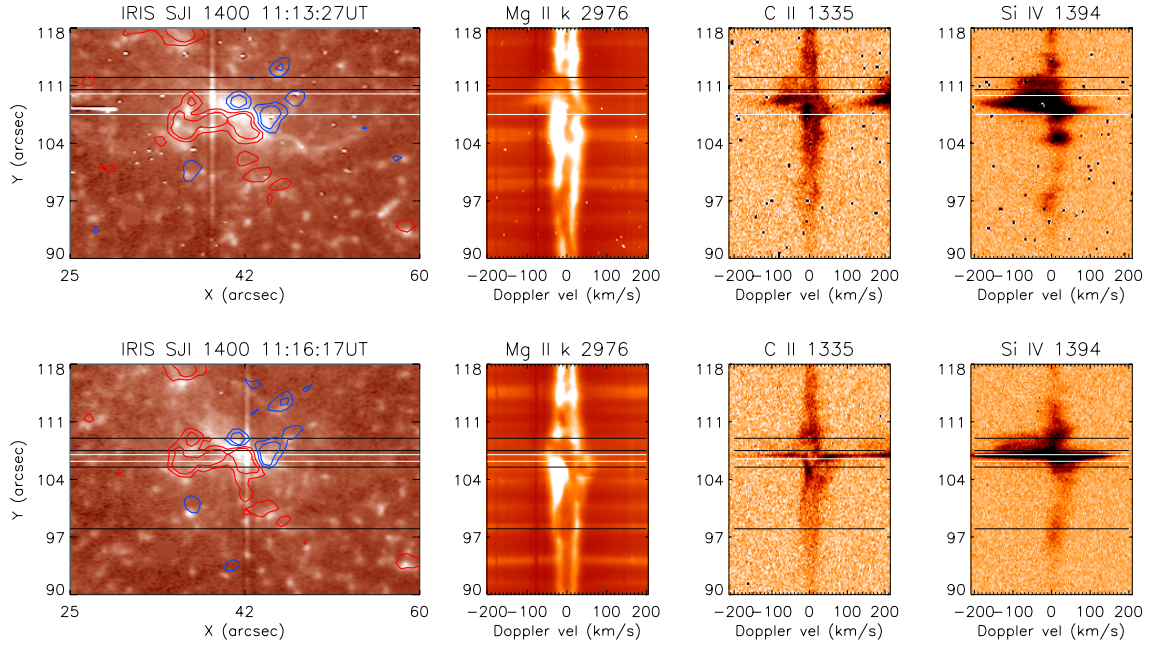
Fig. 5. IRIS SJI 1400 and spectral-slit images while the IRIS slit scans the eruption region (shown from *left to right*). The red and blue contours trace magnetic fluxes at ±50 G. The Mg II k 2796 Å, C II 1335 Å, and Si IV 1394 Å intensity along the IRIS slit are recorded at the times of the IRIS SJI images and at the location seen at the projected IRIS slit on the SJIs. The C II and Si IV spectral-slit images are shown in a reversed colour table. The location between the black horizontal lines is where the mini-filament is recorded, while the part along the slit between the white horizontal lines is the reconnection site area.

emission of up to $20 \, \mathrm{km \, s^{-1}}$ is also clearly seen lower along the slit (see the lower two horizontal black lines) and the intensity decrease in the Mg II k 2796 red-wing is a clear indication that it is related to cool material, namely, the mini-filament. It appears after 11:15:30 UT and it lasts throughout the following scan positions, indicating that some or all of the filament material falls back, which strongly suggest a failed filament eruption. To summarise, the red and blue shift patterns represent the erupting filament that lifts up (blue-shifted) and expands or falls back as time progresses (red-shifted). For full details on the evolution of the erupting filament recorded simultaneously in both the imaging and the spectroscopic data, we refer to the animation in Fig. A.2.

The spectroscopic data also deliver unique observations of the reconnection site. The first is that strong blue- and red-shifted emission from the reconnection site of more than $100 \, \mathrm{km^{-1}}$ (in Si IV 1394) is detected in all lines at 11:12:37 UT (the animation in Fig. A.2). As the slit scans through the outflows and the elongated bright feature, the blue-shifted emission is dominant and slightly offset with respect to the redshift due to the asymmetry of the structure with respect to the spectrometer slit. After the slit enters the location above the cancelling magnetic flux which is presumably the reconnection site, the blue- and red-shifted wings show similar Doppler shifts (see the animation in Fig. A.2 from 11:14:41 UT until 11:17:29 UT). This spectral emission evolution and appearance has been attributed to the so-called explosive events and is discussed further in Sect. 4. The blue-shifted wing in the Si IV line reaches more than $200 \, \mathrm{km \, s^{-1}}$ at 11:14:18 UT. We should mention that the blue wing of the C II line at 1335.71 Å blended with C II 1335.66 Å, enters the shown spectral window when the Doppler shifts in the two wings increase above $135 \, \mathrm{km \, s^{-1}}$ causing the red wing of the C II 1334.53 Å to overlap with the blue wings of C II 1335.71 and C II 1335.66 Å (see the animation in Fig. A.2). A separation of the contribution would be very challenging because the blue wing comes from two lines.

3.3. NLFFF modelling

To study the non-potential evolution of the CBP coronal magnetic field, we simulated a continuous time series of NLFFFs. The NLFFFs are produced using the technique described in the papers of Mackay et al. (2011) and Gibb et al. (2014). In this technique, a time series of HMI line-of-sight magnetograms are directly applied to simulate the boundary driving at the solar photosphere. The initial coronal magnetic field is chosen as a potential magnetic field deduced from the initial magnetogram in the time series. The simulations are carried out in an open and periodic computational box of 512^3 grid points, where the resolution in the vertical direction is set to be twice that used in the horizontal directions. To specify the normal magnetic field component on the lower boundary, a 256^2 HMI pixel region centred on the region of interest is cut out of the HMI magnetograms and then interpolated to 512^2, while conserving flux. This increased resolution is used in the simulations so that small-scale structures in the low solar corona can be resolved, as well as to minimise the effect of numerical diffusion. Due to the application of open-top boundary conditions, no correction for flux balancing is applied and a significant amount of the photospheric flux reaches the top boundary and is defined as open. Then, as the time sequence of normal component magnetograms is applied, the coronal magnetic field responds to these driving motions by evolving through a continuous series of quasi-static NLFFF using the magneto-frictional relaxation technique. The full details of the numerical implementation and the equations solved can be found in the cited papers, along with Papers II and III.

Firstly, we produced a series of NLFFF simulations following the description given in Gibb et al. (2014), where the only injection of energy and non-potentiality into the solar corona arises from the time evolution of the magnetic footpoints deduced from the normal component magnetograms. The

simulations start at 01:58 UT on 5 April 2017 and run until 11:35 UT the same day. The resulting 3D non-potential magnetic field is then analysed at the location of the CBP around the time of the observed eruption (11:00–11:10 UT). These initial simulations failed to produce any strongly sheared or highly non-potential magnetic structures at the location or time of the CBP or MF. In contrast, the field lines maintained a simple nested loop structure normal to the PIL. This structure closely represents what would be expected from a potential field. Subsequent investigation showed that the lack of strongly sheared fields was a consequence of the simple flow patterns of the magnetic elements around the CBP. These flow patterns involved only a simple converging motion of the positive and negative polarities over the time period considered, without any shear flows. Such motions do not inject any axial field along the PIL that would explain the CBP or MF structure but, rather, they merely result in field lines that shrink in length and height while remaining normal to the PIL. As a result, we conclude that for the present example, the observed horizontal motions deduced from the normal component magnetograms, when acting on an initial potential field, cannot inject enough non-potentiality into the coronal field to reproduce the observed phenomena. To investigate the validity of the initial potential field AIA 171, 193, and 211 Å observations taken at 01:58 UT were studied. The visible, albeit faint, coronal loops were then compared to the field lines of the initial potential field. The comparison produced a good agreement between the observations and the potential field model, indicating that there was no pre-existing shear in the field at this time. As such, the discrepancy between the observation and model found at 11:00 UT was not due to the initial condition. At this point, it is important to note that the simulated magnetic features are not fully resolved as their scale is close to the resolution of the HMI magnetograms. As a result, we may speculate that there may be unresolved motions such as shearing motions or vortical flows that lead to a further injection of non-potentiality into the field. Such an additional injection is necessary to explain the highly non-potential field configurations of the CBP and MF seen in the observations.

As the basic approach described above only uses the normal component magnetograms and since it lacks the ability to reproduce the main features of the observations, we considered a number of speculative experiments where additional non-potentiality was injected into the coronal field. Thus, the same potential field initial condition used in the previous experiments at 01:58 UT on 5 April 2017 was taken. Next, while applying the same evolution of the normal field component at the photosphere, an additional axial field is injected into the simulation at the lower boundary by including the term:

$$\frac{\partial \boldsymbol{A}_{\mathrm{h}}}{\partial t} = -\nabla_z \times \nabla_{\mathrm{h}} \left(\zeta B_z \right), \tag{1}$$

where $\boldsymbol{A}_{\mathrm{h}} = (A_x, A_y)$ represents the horizontal components of the magnetic vector potential at the photospheric boundary ($z = 0$), B_z the normal magnetic field component, and ζ the rate of injection of the horizontal magnetic field or twist component, where it has the dimensions of diffusivity. The addition of this term does not alter the evolution of B_z but injects a horizontal magnetic field component given by:

$$\frac{\partial \boldsymbol{B}_{\mathrm{h}}}{\partial t} = -\nabla_{\mathrm{h}} \left(\zeta B_z \right), \tag{2}$$

at the lower boundary which then propagates upwards along the magnetic field lines through the ideal $\boldsymbol{v} \times \boldsymbol{B}$ term in the induction equation. This term only acts where there is a horizontal spatial variation of the quantity ζB_z and injects a horizontal

field at locations where the gradient is strong such as at polarity inversion lines. The sign or twist of the horizontal field that is injected depends on the parameter ζ where a positive (negative) value of ζ leads to the injection of negative (positive) magnetic helicity. This term is mathematically equivalent to that used in Mackay et al. (2014) to simulate the spatially averaged long-term effects of the helicity condensation process of Antiochos (2013) without having to resolve individual convective cells. As the magnetic fragments in the present simulations are close to the resolution of HMI, it is possible that there are unresolved vortical motions below the presently resolved scales. These may provide an additional source of non-potentiality not captured by the previously applied horizontal motions. As a result, we then carry out the following speculative simulations, where an additional non-potential field is injected during the time evolution of the field.

Using the formulation described above along with the time sequence of observed normal component magnetograms, the coronal field is evolved forward from 01:58 UT on 5 April 2017 until 11:35 UT on the same day, using $\zeta = -175\,\mathrm{km^2\,s^{-1}}$. At various points during the evolution, the resulting field configuration was investigated and compared to the observations. The general tendency observed is that the longer the injection, the greater the amount of increased shear was found along the PIL. The three images in Fig. 6 show examples of the resulting field lines around the PIL at 10:58 UT on 5 April 2017. The top image represents the field structure of the extended lower part of the PIL. The middle and bottom frames in Fig. 6 include higher-lying field lines that show a sheared arcade system overlying the PIL. The colour coding of the field lines represents the strength of the current, defined as $\boldsymbol{J} = \nabla \times \boldsymbol{B}$. This indicates that the lower more strongly sheared field lines contain significant current and subsequently free magnetic energy. The strongly sheared field lines closely match the path of the MF, where this free magnetic energy may be used to drive the mini-eruption. One important aspect of the present non-potential field is that there is no magnetic null point identified above the region along the PIL. By running several simulations and varying ζ, we find this to be true no matter how much twist or axial field is injected.

The magnetic field line traces seen in Fig. 6 indicate the presence of a QSL in the vicinity of the PIL between the two converging flux concentrations. This was investigated further using the data shown in Fig. 6. The squashing factor Q values are determined by following the second method in Pariat & Démoulin (2012, Sect. 3.2). Figure 7 shows the log 10 of the derived Q values over the relevant part of the magnetogram. To better depict the location of the high-Q layers, magnetic field contours of the normal photospheric component of the magnetic field at ± 50 G values are also shown. The Q visualisation reveals a complicated spatial distribution of the Q-value in the lower atmosphere. It shows the existence of different complex-shaped high-value Q-layers on either side of the region containing the sheared field lines in Fig. 6. The different frames in Fig. 7 show how the Q structure and spatial location changes with height above the photosphere and how the different structures shift relative to the underlying magnetic field concentrations. From the calculations, it can be seen that the Q-layers for the lowest height are concentrated well within the two converging polarity regions. As expected, with increased height in the atmosphere, they are located closer to the projected PIL. It is also found that the Q-layers extend in the southeast direction relative to the closest approach of the two flux concentrations.
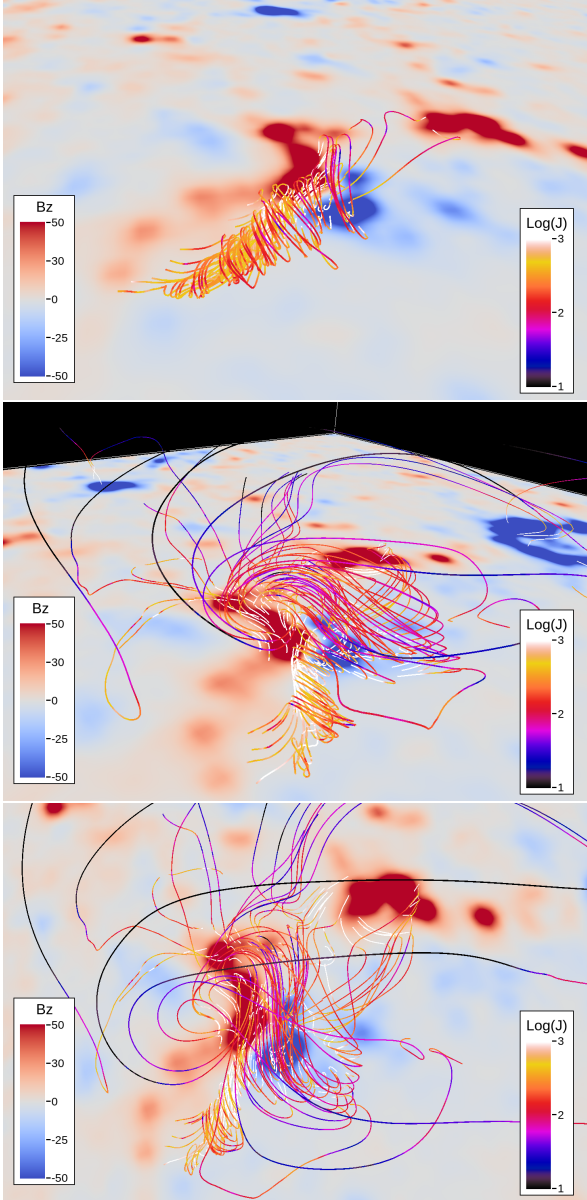
Fig. 6. Illustrations of the field lines above the polarity inversion line for the simulation where $\zeta = -175 \, \mathrm{km}^2 \, \mathrm{s}^{-1}$ at 10:58 UT on 5 April 2017. The field lines are shown at low (*top*) and high (*middle* and *bottom*) heights above the PIL. The colour coding represents the strength of the electric current, defined as $\boldsymbol{J} = \nabla \times \boldsymbol{B}$ along the field lines as given in the right-hand side (Log(J) ranging from 1 to 3). The background image represents the photospheric magnetogram where red represents positive flux and blue negative flux in the range $\pm 50 \, \mathrm{G}$, left-hand sub-panel.

4. Discussion

Small-scale eruptions also known as mini-CMEs in the quiet Sun are now known to be omnipresent, with as many as 1400 per day over the whole Sun (Innes et al. 2009). No less than 870 of them are believed to be related to CBPs (Paper I). These small-scale eruptions eject both cool and hot plasma into the upper atmosphere and are expected to have a certain (maybe even significant) contribution to the energy and mass balance of the solar atmosphere. Here, we used unique imaging and spectral co-observations to investigate the nature of one of these dynamic phenomena and, more specifically, the physical processes involved in them. We report IRIS (both spectroscopic
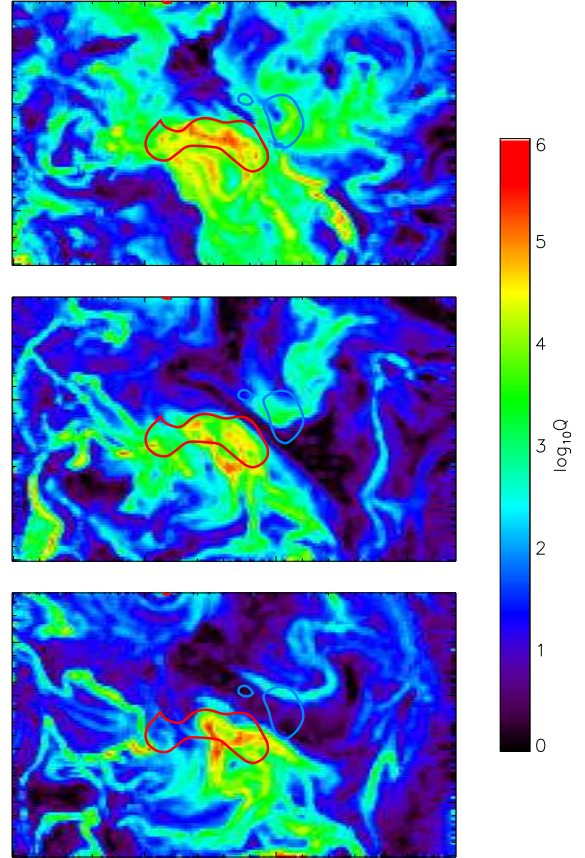

Fig. 7. Three frames showing the spatial distribution of the derived $\log_{10}Q$ values in different horizontal planes above the magnetogram surface. The *top panel* corresponds to a plane at a height of 110 km, the *middle* at 1105 km, and the *bottom* at 2764 km. The blue and red contours denote the negative and positive photospheric magnetic field, respectively at values of $B_z = \pm 50 \, \mathrm{G}$. The images are smoothed with a boxcar of width $3 \times 3 \, \mathrm{px}^2$.

and imaging) and AIA observations of a mini-filament eruption and a micro-flare. The appearance of an elongated bright feature whose J-shaped edges wrap around the footpoints of the erupting mini-filament strongly suggests reconnection in a quasi-separatrix layer (QSL) formed through the convergence of small-scale magnetic polarities. These polarities observed in the HMI magnetograms strongly resemble their large counterparts in active regions.

These observations also reveal important details on the properties of these eruptions, including a relation of the reconnection driven outflows seen in the IRIS imaging and spectroscopic data to 'explosive events'. As mentioned in Sect. 3.2, the spectral-line profiles detected while crossing the eruption site are usually attributed to these so-called 'explosive events'. Explosive events were discovered by Brueckner & Bartoe (1983) in C IV 1548.21 Å in spectra taken with the high-resolution telescope and spectrometer (HRTS) and were first called turbulent events. As the term 'turbulent' did not appear to describe the observed spectral-line widths, they were then named 'explosive events' (EEs) (Dere et al. 1984, 1986, 1989). These EEs display strong blue and red-shifted emission, where often the blue emission is stronger than the red, and the line profiles can be either Gaussian or non-Gaussian. They are short-lived (60–350 s) but often appear in bursts continuing for as long as 30 min in regions undergoing magnetic cancellation (e.g. Dere 1994; Chae et al. 1998).

Their sizes, determined along a spectrometer slit, are 3″–5″. They display Doppler shifts of up to 200 km s^{-1}. Dere et al. (1991) first suggested that this should be the spectroscopic signature of high-velocity bi-directional plasma ejections during magnetic reconnection. Chae et al. (1998) associated EEs with mixed magnetic polarity or found them at the border of regions with a large concentration of magnetic flux. These authors reported that out of 163 EEs, 103 occurred above areas of magnetic-flux cancellation. The EEs were also registered in data taken by the SUMER spectrometer and IRIS (e.g. Innes et al. 1997; Huang et al. 2014). More details on the background of EEs can be found in Huang et al. (2014). From the EE description above, it became swiftly evident that the spectroscopic observations presented here display an EE. The EE indeed represents bi-directional flows from a reconnection site, but these outflows do not solely contribute to the EE emission. The IRIS and AIA imaging information indicates the contribution from an erupting mini-filament and eventually chromospheric evaporation of gentle type have contributed to the EE, namely, non-Gaussian spectral line profiles.

The evolution of the mini-eruption described here involving an elongated bright feature with J-shaped edges seen in the EUV (for details, see Sect. 3.1) follows the flux cancellation CME model of Aulanier et al. (2010) very closely. This model was inspired by the observations of the evolution of cancelling bipolar magnetic flux in active regions. The cancellation observed here (see animation in Fig. A.1) is without any doubt very similar to active region flux cancellation but on a much smaller scale. Numerous models have demonstrated the formation of sheared magnetic flux due to magnetic flux cancellation along the polarity inversion line or the shearing of arcade field lines (e.g. Mackay et al. 2010, and references therein). It has long been suggested that CBPs represent scaled-down active regions. During the late stages of the CBPs lifetime, the magnetic bipoles that sustain these phenomena are observed to cancel in the majority of the cases (for details see Mou et al. 2016). Eruptions in active regions also typically occur in the late stage of the AR lifetime, the so-called decay phase (e.g. Démoulin et al. 2002; Green & Kliem 2009). The mini-filaments' formation and evolution reported in Mou et al. (2018), as well as the event described in the present study also strongly support this similarity. Because of the small scale of the observed feature and the small number of pixels of its resolution in the observations, some details cannot be observed or derived from the modelling, which is discussed in detail in Sect. 3.3. Surprisingly similarly to the model, the photospheric magnetic flux shows a decrease of 24% during the three consecutive eruptions.

The narrow elongated feature with J-shaped edges (sigmoid-like) with a width of only 0.34″ (~250 km), as seen in the IRIS SJ 1400 images, presumably represents the newly reconnected loops. It is nearly a pixel (IRIS) sized brightening that is identified as the micro-flare initial reconnection site. The brightening quickly spreads bi-directionally along the elongated feature. An investigation of the imaging information from all AIA channels analysed here indicates emission from plasmas heated to up to several million degrees (Fe XVIII, 7 MK formation temperature). The highest (AIA 94) temperature emission is localised in a smaller area than the rest of the high-temperature emission (AIA 171 and AIA 193). Both edges of the elongated structure curl into a J-shaped feature (hook-like) creating the appearance of a sigmoid at the end of which plasma outflows are observed and are best seen in the IRIS SJIs (see Fig. A.1). This coincides with the lift-off of the erupting mini-filament with the hooks' located at both ends of the mini-filament. Savcheva et al. (2012)

compared the geometrical and topological properties of sigmoidal active region CME involving a filament using an NLFFF model and high-resolution magneto-hydrodynamic (MHD) simulations. The study established that in both the MHD simulations and the observed magnetic field evolution derived from the NLFFF model, flux cancellation plays a fundamental role in building the magnetic flux rope. The main QSLs were found to wrap around the edges of the flux rope. The investigation also showed the existence of hyperbolic flux tubes (HFTs) (Titov 2007) in the MHD models in vertical cross-sections of the computed squashing factor, with the main HFT located under the sheared flux rope in both models. This HFT was identified as the most probable site for reconnection. From their torus instability analysis Savcheva et al. (2012) concluded that the eruption of the flux rope was caused by the combination of the flux rope expanding in a torus instability domain together with magnetic reconnection in the HFT. The mini-filament slowly rises for approximately 6 min (see Table 1), followed by a brusque liftoff. This may have been caused by the interplay of the magnetic reconnection and a torus (e.g. Démoulin & Aulanier 2010; Kliem & Török 2006) or kink instability (Kliem et al. 2004; Török & Kliem 2005). Due to the small scale of the erupting filament in comparison to large eruptions (e.g. Koleva et al. 2012, and reference therein), it is impossible to say in the present case whether one or the other instability has played a role in the destabilisation and eruption. The scenario of QSL reconnection involving a filament is described by Janvier et al. (2014, and references therein) with a cartoon illustration shown in Fig. 7. Visualisation of the vertical current layer with clearly distinguishable hooks is shown in Fig. 11 of Kliem et al. (2013). The signature of the micro-flare, detected as intense brightening localised in just a few pixels, is observed below the rising mini-filament. As shown in Paper III, this implies that high energy release, presumably from magnetic reconnection, triggered by the rising mini-filament results in the heating of the chromospheric plasma to high temperatures causing the appearance of (micro-)flare ribbons (unresolved here due to resolution limitations) beneath the rising filament as shown in detail in Paper III.

The squashing factor Q investigation is based on the advected and vortex imposed NLFFF modelling and shows the presence of a number of QSLs in the region around the PIL between the two converging flux concentrations (see Fig. 7). These QSLs nicely align with the sheared flux tube identified in Fig. 6. Despite the somewhat 'artificial' approach in obtaining this field line configuration, it clearly indicates that the sheared field structure is embedded in a QSL that defines a possible location where magnetic reconnection between a rising flux rope and the ambient magnetic field may take place – leading to the general action discussed from the combined observations. Imposing an artificial twist to the magnetic field to build up the flux-rope magnetic structure was required because of the limitations of the available observations. In the future, we hope that ground-based observations from, for instance, the Visible Spector-Polarimeter on *Daniel K. Inouye* Solar Telescope (DKIST) at a resolution as low as 50 km may help resolve the fine details of the photospheric and coronal magnetic field evolution so it may be better modelled.

Some of the detected upflows (blue-shifted emission) in the chromospheric and transition-region lines may be related to chromospheric evaporation. Due to the small scale of the event, it is impossible to precisely separate the emission from the reconnection site, chromospheric evaporation, and erupting mini-filament. Recently, Frogner et al. (2020) demonstrated that particle beams in the quiet Sun, especially those from

micro-flares as in the case studied here, can cause chromospheric heating. This would lead to chromospheric evaporation, so although this assumption is speculative, in our view, the presence of chromospheric evaporation is very plausible. If the data had been taken in a sit-and-stare mode, we may perhaps have been able to say more and with a greater degree of certainty, as in Gömöry et al. (2016) for a large filament eruption. The other challenge is the size of the event or, rather, the resolution of the present instrumentation. The spectral data analysis shows, however, a lack of a distinctive red-shifted emission in the transition-region and chromospheric lines as commonly observed during explosive chromospheric evaporation. This hints at the possible presence of gentle chromospheric evaporation based on the interpretation of the detected lower velocity upflows. It was estimated by Fisher et al. (1985) that when the energy flux during flares is lower than ~10^{10} ergs cm^{-2} s^{-1}, the heating of the chromosphere would lead to gentle evaporation upflows in a wide range of temperatures and at a speed of several tens of km s^{-1} with no accompanied downflows. Typically, gentle evaporation is reported during the decay phase of solar flares and relates to plasma heated by thermal conduction during this phase (e.g. Zarro & Lemen 1988; Berlicki et al. 2005). Milligan et al. (2006) reported observing gentle evaporation during the impulsive phase of a C9.1 flare that was driven by non-thermal electrons. Figure 4 in Milligan et al. (2006) demonstrates the difference in the Doppler velocity in spectral lines with different temperatures with blue-shift in the case of gentle evaporation and red-shift in the case of an explosive one in transition region lines. IRIS does not have strong enough coronal lines to account for the line shifts at coronal temperatures. A forthcoming study by Hannah et al. (in prep.) reports the detection of hard X-ray emission in the 2.5−4 keV (stronger) and 4−6 keV (much weaker) by the Nuclear Spectroscopic Telescope Array (*NuSTAR*) in an event similar to the one described here, confirming the presence of micro-flares in small-scale eruptions in the quiet Sun which would trigger gentle chromospheric evaporation. We hope to detect a few more of these events in IRIS data so we can deliver further details especially on the detection of chromospheric evaporation during small-scale eruptions in the quiet Sun.

5. Summary and conclusions

This paper reports on the investigation of an eruption from a coronal bright point associated with a mini-filament eruption and cancelling magnetic fluxes of opposite polarities (Fig. 1). Remarkably, all the phenomena were recorded in both the imaging and spectroscopic data of the Interface Region Imaging Spectrograph (IRIS). We identified an intense small-scale brightening as a micro-flare, followed by the mini-eruption associated with the ejection of the CBP loops and mini-filament plasmas (Fig. 2 and animation in Fig. A.1). The mini-filament eruption is seen in the spectroscopic IRIS data as spectral-line shifts (stronger blue- and weaker red-shifts) of the Mg II, C II, and Si IV lines (Figs. 4 and 5). An elongated bright feature (located above the polarity inversion line) that is only visible in the IRIS slit-jaw 1400 Å images appears shortly before the micro-flare. This feature appears to represent the newly reconnected loops. The micro-flare starts with an IRIS pixel size brightening and propagates bi-directionally along the elongated feature (animation in Fig. A.1). We found strong (out)flows along and at the edges of the elongated feature in both the spectral and imaging IRIS data and AIA data which we believe represent the reconnection outflow. The observed red-shifted emission is seemingly related to the falling back mini-filament's plasmas. The edges

of the elongated feature expand into a J-shaped feature creating the appearance of a sigmoid. A number of high valued Q structures are found in the region around the PIL separating the two converging flux concentrations. As coronal null points were not found above the converging and cancelling magnetic polarities, the high-value Q-regions must represent QSLs in the vicinity of the sheared magnetic flux.

The present study uses unique IRIS observations of an eruption from a CBP and provides further observational and modelling evidence that CBPs are downscaled active regions where magnetic reconnection along QSLs, (mini-)filament eruptions, (mini-)CMEs or jets, (micro-)flaring, (gentle-)chromospheric evaporation, and similar events occur. The QSL reconnection site is presented in the spectroscopic data as the location of so-called explosive events (EEs, non-Gaussian profiles) identified by strong blue- and red-shifted emission of up to 200 km s^{-1} thus demonstrating the EEs are indeed witnessing magnetic reconnection-driven plasma flows. A forthcoming study will report on the occurrence rate of mini-eruptions related to QSL reconnection in the quiet Sun and their plasma and observational properties.

References

Antiochos, S. K. 2013, ApJ, 772, 72
Aulanier, G., Török, T., Démoulin, P., & DeLuca, E. E. 2010, ApJ, 708, 314
Benz, A. O. 2017, Liv. Rev. Sol. Phys., 14, 2
Berlicki, A., Heinzel, P., Schmieder, B., Mein, P., & Mein, N. 2005, A&A, 430, 679
Brueckner, G. E., & Bartoe, J. D. F. 1983, ApJ, 272, 329
Chae, J., Wang, H., Lee, C.-Y., Goode, P. R., & Schühle, U. 1998, ApJ, 504, L123
Cirigliano, D., Vial, J. C., & Rovira, M. 2004, Sol. Phys., 223, 95
De Pontieu, B., Title, A. M., Lemen, J. R., et al. 2014, Sol. Phys., 289, 2733
Del Zanna, G. 2013, A&A, 558, A73
Démoulin, P., & Aulanier, G. 2010, ApJ, 718, 1388
Démoulin, P., Priest, E. R., & Lonie, D. P. 1996, J. Geophys. Res., 101, 7631
Démoulin, P., Mandrini, C. H., van Driel-Gesztelyi, L., et al. 2002, A&A, 382, 650
Dere, K. P. 1994, Adv. Space Res., 14, 13
Dere, K. P., Bartoe, J. D. F., & Brueckner, G. E. 1984, ApJ, 281, 870
Dere, K. P., Bartoe, J. D. F., & Brueckner, G. E. 1986, ApJ, 310, 456
Dere, K. P., Bartoe, J. D. F., & Brueckner, G. E. 1989, Sol. Phys., 123, 41
Dere, K. P., Bartoe, J. D. F., Brueckner, G. E., Ewing, J., & Lund, P. 1991, J. Geophys. Res., 96, 9399
Fisher, G. H., Canfield, R. C., & McClymont, A. N. 1985, ApJ, 289, 434
Fletcher, L., Dennis, B. R., Hudson, H. S., et al. 2011, Space Sci. Rev., 159, 19
Frogner, L., Gudiksen, B. V., & Bakke, H. 2020, A&A, 643, A27
Galsgaard, K., Madjarska, M. S., Mackay, D. H., & Mou, C. 2019, A&A, 623, A78
Gibb, G. P. S., Mackay, D. H., Green, L. M., & Meyer, K. A. 2014, ApJ, 782, 71
Gömöry, P., Veronig, A. M., Su, Y., Temmer, M., & Thalmann, J. K. 2016, A&A, 588, A6
Green, L. M., & Kliem, B. 2009, ApJ, 700, L83
Green, L. M., Kliem, B., & Wallace, A. J. 2011, A&A, 526, A2
Hermans, L. M., & Martin, S. F. 1986, NASA Conf. Publ., 2442, 369
Huang, Z., Madjarska, M. S., Xia, L., et al. 2014, ApJ, 797, 88

Innes, D. E., Inhester, B., Axford, W. I., & Wilhelm, K. 1997, Nature, 386, 811
Innes, D. E., Genetelli, A., Attie, R., & Potts, H. E. 2009, A&A, 495, 319
Innes, D. E., McIntosh, S. W., & Pietarila, A. 2010, A&A, 517, L7
Janvier, M., Aulanier, G., Bommier, V., et al. 2014, ApJ, 788, 60
Joshi, B., Kushwaha, U., Veronig, A. M., et al. 2017, ApJ, 834, 42
Kliem, B., & Török, T. 2006, Phys. Rev. Lett., 96, 255002p
Kliem, B., Titov, V. S., & Török, T. 2004, A&A, 413, L23
Kliem, B., Su, Y. N., van Ballegooijen, A. A., & DeLuca, E. E. 2013, ApJ, 779, 129
Koleva, K., Madjarska, M. S., Duchlev, P., et al. 2012, A&A, 540, A127
Leenaarts, J., Pereira, T. M. D., Carlsson, M., Uitenbroek, H., & De Pontieu, B. 2013, ApJ, 772, 90
Lemen, J. R., Title, A. M., Akin, D. J., et al. 2012, Sol. Phys., 275, 17
Mackay, D. H., Karpen, J. T., Ballester, J. L., Schmieder, B., & Aulanier, G. 2010, Space Sci. Rev., 151, 333
Mackay, D. H., Green, L. M., & van Ballegooijen, A. 2011, ApJ, 729, 97
Mackay, D. H., DeVore, C. R., & Antiochos, S. K. 2014, ApJ, 784, 164
Madjarska, M. S. 2019, Liv. Rev. Sol. Phys., 16, 2
Madjarska, M. S., Vial, J. C., Bocchialini, K., & Dermendjiev, V. N. 1999, in 8th SOHO Workshop: Plasma Dynamics and Diagnostics in the Solar Transition Region and Corona, eds. J. C. Vial, & B. Kaldeich-Schü, ESA Spec. Publ., 446, 467

Madjarska, M. S., Doyle, J. G., & Shetye, J. 2015, A&A, 575, A39
Madjarska, M. S., Galsgaard, K., Mackay, D. H., Koleva, K., & Dechev, M. 2020, A&A, 643, A19
Madjarska, M. S., Chae, J., Moreno-Insertis, F., et al. 2021, A&A, 646, A107
Milligan, R. O., Gallagher, P. T., Mathioudakis, M., & Keenan, F. P. 2006, ApJ, 642, L169
Mou, C., Huang, Z., Xia, L., et al. 2016, ApJ, 818, 9
Mou, C., Madjarska, M. S., Galsgaard, K., & Xia, L. 2018, A&A, 619, A55
O'Dwyer, B., Del Zanna, G., Mason, H. E., Weber, M. A., & Tripathi, D. 2010, A&A, 521, A21
Parenti, S. 2014, Liv. Rev. Sol. Phys., 11, 1
Pariat, E., & Démoulin, P. 2012, A&A, 541, A78
Pesnell, W. D., Thompson, B. J., & Chamberlin, P. C. 2012, Sol. Phys., 275, 3
Rathore, B., Carlsson, M., Leenaarts, J., & De Pontieu, B. 2015, ApJ, 811, 81
Rust, D. M., & Kumar, A. 1996, ApJ, 464, L199
Savcheva, A., Pariat, E., van Ballegooijen, A., Aulanier, G., & DeLuca, E. 2012, ApJ, 750, 15
Scherrer, P. H., Schou, J., Bush, R. I., et al. 2012, Sol. Phys., 275, 207
Titov, V. S. 2007, ApJ, 660, 863
Török, T., & Kliem, B. 2005, ApJ, 630, L97
Zarro, D. M., & Lemen, J. R. 1988, ApJ, 329, 456
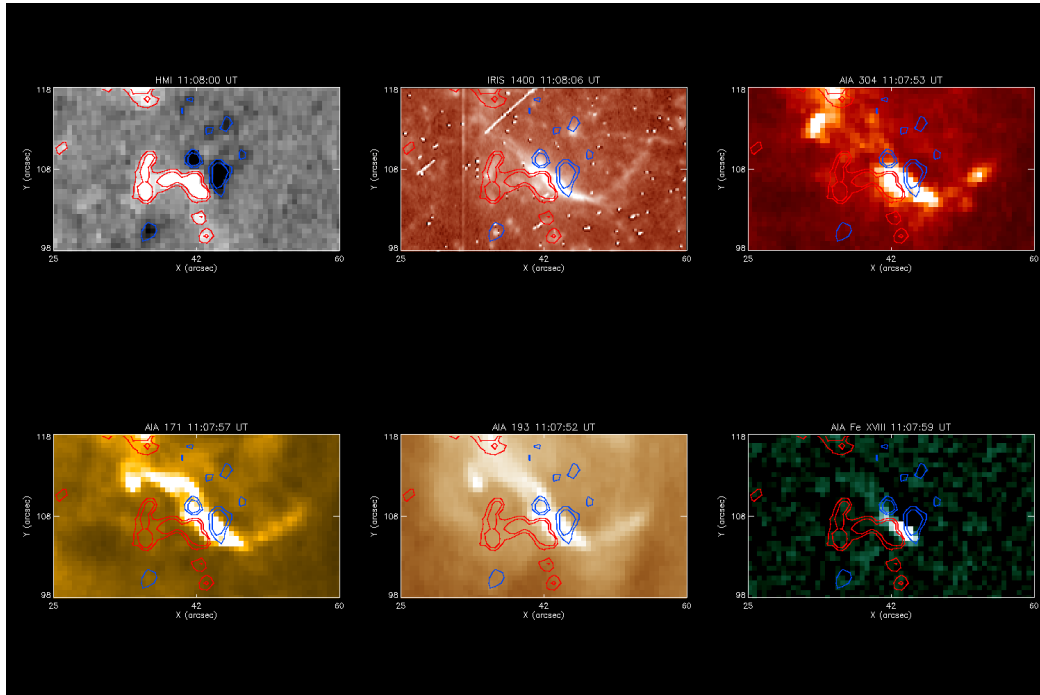
Appendix A: Online material

Fig. A.1. Quasi-temporal animation. *From left to right, top and bottom:* HMI magnetogram, IRIS SJI 1400, AIA 304, 171, 193, and Fe XVIII (see the text for details). The red and blue contours trace magnetic fluxes at ±25 G and ±50 G.
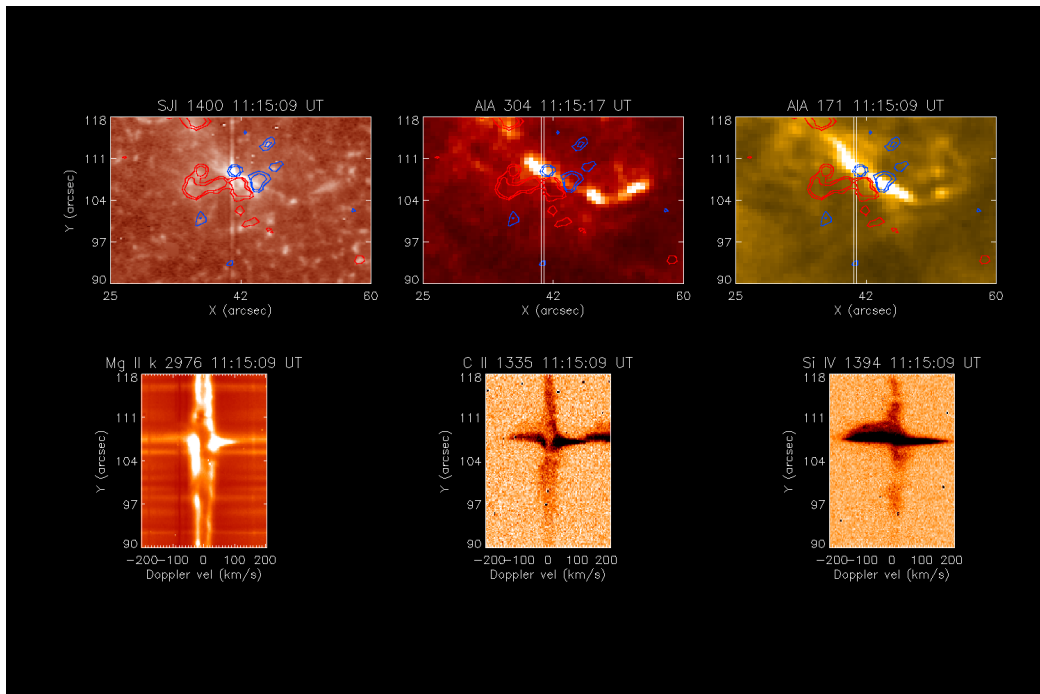

Fig. A.2. Co-temporal animation of imaging and spectral slit data: *Top:* IRIS SJI 1400, AIA 304 and 171 images. The red and blue contours trace magnetic fluxes at ±25 G and ±50 G. *Bottom:* Mg II k 2796, C II 1335, and Si IV 1394 intensity images along the IRIS slit. The position of the slit is visible as a vertical strip on the SJI 1400, and is overplotted as two vertical lines on the AIA 304 and 171 images.